Turkish Journal of Chemistry
http://journals.tubitak.gov.tr/chem/
Research Article

Turk J Chem
(2018) 42: 472 – 481
© TÜBİTAK
doi:10.3906/kim-1709-60

# Influence of manganese content on the supercapacitive performance of $PbO_2$–$MnO_2$ electrodes

**Yingwu YAO[1,*], Mengyao LI[1], Xinghua ZHANG[2], Zunming LU[2], Feng WEI[1]**
[1]School of Chemical Engineering and Technology, Hebei University of Technology, Tianjin, P.R. China
[2]School of Materials Science and Engineering, Hebei University of Technology, Tianjin, P.R. China

**Received:** 28.09.2017 • **Accepted/Published Online:** 11.12.2017 • **Final Version:** 27.04.2018

**Abstract:** $PbO_2$–$MnO_2$ electrodes were prepared by electrochemical codeposition methods. The electrodes were characterized by scanning electron microscope, X-ray photoelectron spectroscopy, energy dispersive X-ray spectroscopy, and X-ray diffraction. The content of manganese in the electrodes increased with the increase in manganese ion concentration in the solution, which can reach 48.4%. The codeposition of manganese decreased the grain sizes and formed the porous structure. Cyclic voltammetry and galvanostatic charge–discharge measurements were used to evaluate the influence of manganese content in the electrodes on the specific capacitive performance of $PbO_2$–$MnO_2$ electrodes. The specific capacitance of $PbO_2$–$MnO_2$ (48.4%) electrodes could reach 374.5 F $g^{-1}$. The excellent specific capacitance can be ascribed to the porous structure and the synergy of excellent conductivity of lead dioxide and the good specific capacitance of manganese dioxide.

**Key words:** $PbO_2$–$MnO_2$ electrodes, manganese content, porous structure, supercapacitive property

## 1. Introduction

Supercapacitors are important energy storage devices that have attracted more and more attention due to their long cycle life, high energy density, and fast charging–discharging performance.[1] The capacitive performance of supercapacitors greatly depends on the positive materials. Metal oxides have been considered promising positive materials of supercapacitors for their low cost and high specific capacitance.[2]

$PbO_2$ electrodes prepared by electrodeposition methods possess high conductivity and excellent chemical stability, which can be used as positive materials.[3] Egan et al. prepared lead dioxide electrodes with nanostructure for a lightweight lead-acid battery.[4] Sáeza et al. studied the electrocrystallization mechanism of lead dioxide on glassy carbon electrodes.[5] Moncada et al. prepared $PbO_2$ nanowires by the template method.[6] Yang et al. obtained free-standing $PbO_2$ nanowires on titanium foil and studied the electrochemical behavior of $PbO_2$ nanowire electrodes.[7] Velichenko et al. prepared lead dioxide electrodes from methanesulfonic solution and studied their physicochemical properties.[8] Ghasemi et al. investigated the energy storage capacity of nanostructured lead dioxide formed by pulsed current.[9] Gao et al. designed the hybrid supercapacitors with $PbO_2$ thin films as positive materials, which show high power and cycle performance.[10] It is worth noting that the conductivity of $PbO_2$ is excellent,[11] but the specific capacitance of $PbO_2$ is lower than that of transition metal oxides, such as $MnO_2$ and NiO. Therefore, combining $PbO_2$ with highly specific capacitive transition

*Correspondence: yaoyingwu@hebut.edu.cn

metal oxides to synthesize new positive materials is an effective way to further improve the specific capacitance of $PbO_2$ electrodes.[12]

$MnO_2$ was also regarded as a promising positive material for supercapacitors,[13] which can be prepared by electrodeposition methods.[14] The theoretical capacitance of $MnO_2$ can reach 1387 F $g^{-1}$, but the practical capacitance was severely limited by the intrinsically poor electrical conductivity of $MnO_2$.[15] It can be assumed to obtain novel binary metal oxides containing $PbO_2$ and $MnO_2$, which should possess the merits of both metal oxides and have excellent pesudocapacitance property,[16] because $PbO_2$ can enhance the conductivity of $MnO_2$ and $MnO_2$ can impart the high capacitance to $PbO_2$.

In the present study, $PbO_2$–$MnO_2$ electrodes were obtained by electrochemical codeposition methods through the addition of manganese nitrate to lead nitrate solution. The morphology, composition, and structure of the $PbO_2$–$MnO_2$ electrodes were analyzed by scanning electron microscope (SEM), X-ray photoelectron spectroscopy (XPS), energy dispersive X-ray spectroscopy (EDS), and X-ray diffraction (XRD). Cyclic voltammetry (CV) and galvanostatic charge–discharge (GCD) measurements were used to evaluate the influence of manganese content in the electrodes on the specific capacitive performance of the $PbO_2$–$MnO_2$ electrodes in 1 mol $L^{-1}$ $H_2SO_4$ solution.

## 2. Results and discussion

### 2.1. Surface morphology and characterization

Figure 1 shows the relation of manganese ion concentration in the bath and the manganese content in the $PbO_2$–$MnO_2$ electrodes. The content of manganese in the electrodes increased with the increase in manganese ion concentration in the solution. The content of manganese in the electrodes reached 48.4% when the manganese ion concentration in the bath was 50 mmol $L^{-1}$. These electrodes can be labeled as $PbO_2$–$MnO_2$ (10.8%), $PbO_2$–$MnO_2$ (32.8%), and $PbO_2$–$MnO_2$ (48.4%) electrodes, based on the manganese content in the $PbO_2$–$MnO_2$ electrodes.

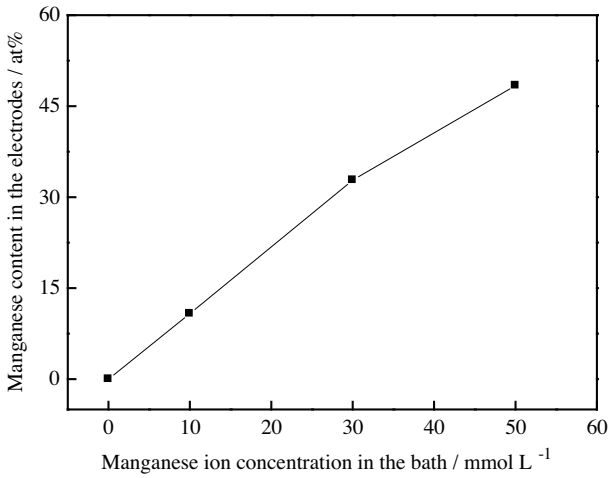


**Figure 1**. The influence of manganese ion concentration in the solution on the manganese content in the $PbO_2$–$MnO_2$ electrodes.

Figure 2 shows the SEM images of pure $PbO_2$ electrodes and different $PbO_2$–$MnO_2$ electrodes. It can be seen from Figure 2a that the pure $PbO_2$ electrodes presented a pyramid shape. Figures 2b–2d show that

with the codeposition of manganese the $PbO_2$–$MnO_2$ electrodes became porous. The pores are interconnected, the walls are composed of numerous particles, and the diameters of particles become smaller with the increase in manganese content in the electrodes. The porous structure can provide a continuous channel to ensure good electrical contact and facilitate ion transport. Furthermore, the porous structure can enlarge the active surface area and enhance the specific capacitance of electrode materials.[17]

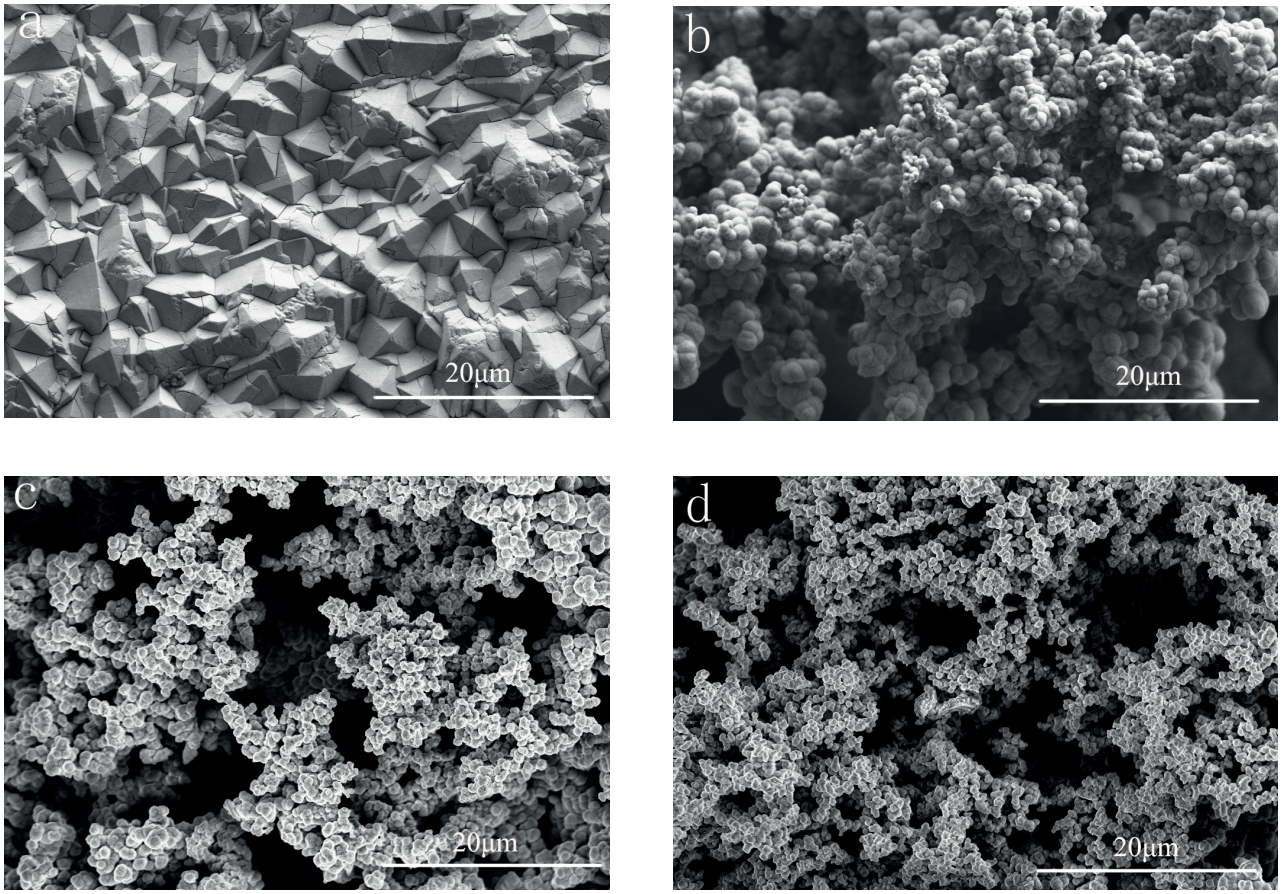


**Figure 2**. Surface morphology of (a) pure $PbO_2$ electrodes, (b) $PbO_2$–$MnO_2$ (10.8%) electrodes, (c) $PbO_2$–$MnO_2$ (32.8%) electrodes, and (d) $PbO_2$–$MnO_2$ (48.4%) electrodes.

The XRD patterns of pure $PbO_2$ and $PbO_2$–$MnO_2$ (48.4%) electrodes are shown in Figures 3a and 3b. The diffraction peaks for pure $PbO_2$ electrodes at 25.3°, 32.1°, and 49.2° correspond to (110), (101), and (211) planes of $\beta$-$PbO_2$, and the diffraction peak at 28.4° corresponds to (111) planes of $\alpha$-$PbO_2$. The codeposition of manganese changes the crystallographic phase. $PbO_2$–$MnO_2$ (48.4%) electrodes contain $\alpha$-$MnO_2$ and $\beta$-$PbO_2$ phases. The diffraction peaks at 32.1°, 36.8°, and 49.2° can be indexed as the planes of $\beta$-$PbO_2$, and the diffraction peaks at 25.8° and 60.3° can be indexed as the planes of $\alpha$-$MnO_2$.[18] All of these peaks are weak and broad, which proves that the crystallinity is relatively poor. The crystal size of $PbO_2$–$MnO_2$ (48.4%) electrodes is 5.2 nm, which is smaller than that of pure $PbO_2$, 24.8 nm.

Figure 4a shows the surface chemical state of $PbO_2$–$MnO_2$ (48.4%) electrodes. The survey spectrum proves the presence of Pb, O, and Mn. Figure 4b shows peaks at 137.8 eV and 142.6 eV, which correspond to Pb $4f_{7/2}$ and Pb $4f_{5/2}$. The peak position shows the spectral values for $PbO_2$. The binding energy between the

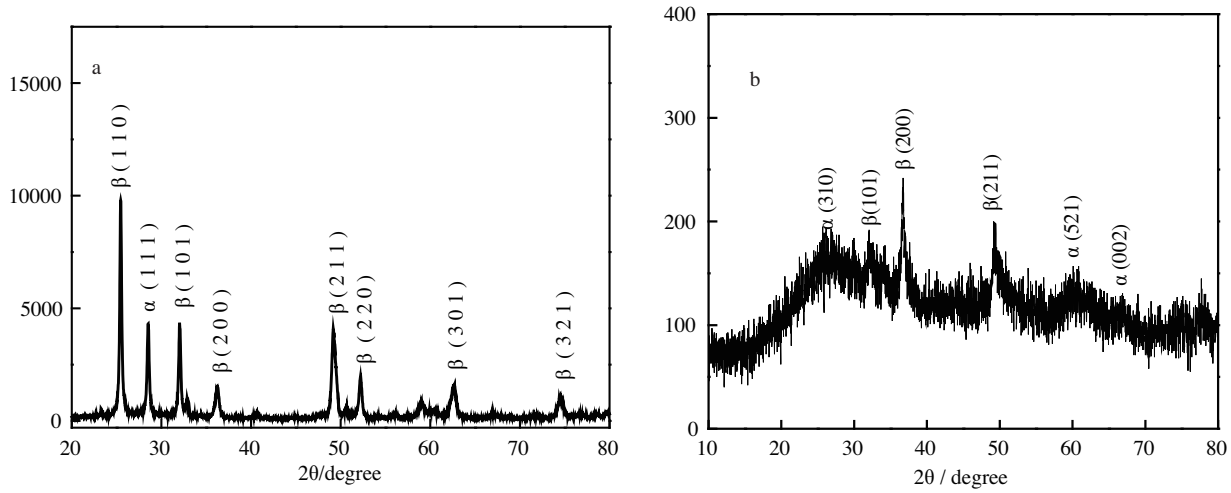


**Figure 3**. XRD patterns of pure $PbO_2$ and $PbO_2$–$MnO_2$ (48.4%) electrodes.

two peaks is 4.8 eV.[19] The XPS peaks of O 1s band (Figure 4c) at 529.6 eV can be found. Both the Mn $2p_{3/2}$ peak at 641.8 eV and Mn $2p_{1/2}$ peak at 653.5 eV can be clearly observed in Figure 4d. The peak separation is 11.7 eV, which indicate that the oxidation state for Mn is $Mn^{4+}$ and $MnO_2$ forms in the composites.[20]

### 2.2. Electrochemical property

The influence of manganese content in the composites on the electrochemical property of $PbO_2$–$MnO_2$ electrodes was measured by cyclic voltammetry in 1.0 mol $L^{-1}$ $H_2SO_4$ solution. Figure 5 compares the cyclic voltammograms of pure $PbO_2$ electrodes and $PbO_2$–$MnO_2$ electrodes with different manganese contents at 10 mV $s^{-1}$. A pair of oxidation–reduction peaks can be observed for pure $PbO_2$ electrodes, which indicates that the capacitive characteristics are mainly governed by faradic reactions.[21] The charge process of the pure $PbO_2$ electrode is associated with the oxidation peak, which is attributed to the oxidation of $PbSO_4$. The discharge process is associated with the reduction peak, which is attributed to the reduction of $PbO_2$. The corresponding electron transfer reaction is illustrated as follows:[22]

$$PbSO_4 + 2H_2O \leftrightarrow PbO_2 + HSO_4^- + 3H^+ + 2e^-$$

The curve shapes of $PbO_2$–$MnO_2$ electrodes are similar to those of pure $PbO_2$ electrodes. However, compared with pure $PbO_2$ electrodes, larger redox peak current densities and curve enclosed areas can be observed for $PbO_2$–$MnO_2$ electrodes. Moreover, the peak current densities and curve enclosed areas increase with the increase in manganese content in the electrodes. It revealed that the specific capacitance of $PbO_2$–$MnO_2$ electrodes should increase with the increase in manganese content in the electrodes.

Electrochemical activity is related to the real surface area per apparent geometric area.[23] The voltammetric charge (q*) is the reflection of the real surface area. The total electrochemical surface area ($q_T$*) can be obtained by plotting the reciprocal of q* against the square root of the scan rate by using the following equation:[24,25]

$$(q^*)^{-1} = (q_T^*)^{-1} + kv^{1/2} \quad (1)$$

The relationship between reciprocal voltammetric charge $(q^*)^{-1}$ and the square root of different scan rate

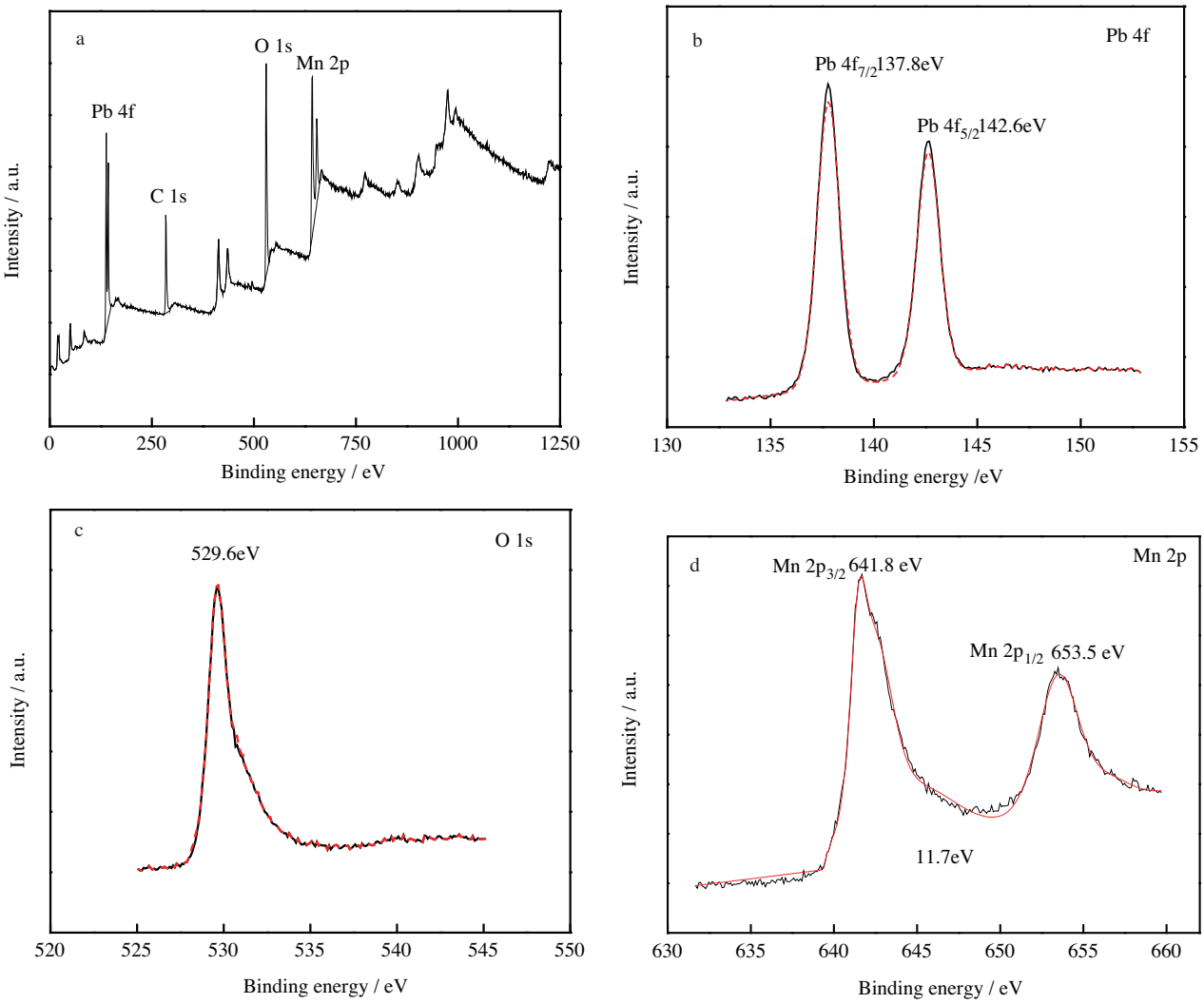


**Figure 4**. XPS spectra of $PbO_2$–$MnO_2$ (48.4%) electrodes: (a) survey spectrum, (b) Pb 4f, (c) O 1s, and (d) Mn 2p.

($v^{1/2}$) for both electrodes is shown in Figure 6. The q* in the pseudocapacitance region can be defined as the electrochemical active surface area (EASA). Through extrapolating the linear plot to v = 0, the total electrochemical surface area $q_T$* can be obtained.[26] The Table shows that all the voltammetric charge values of $PbO_2$–$MnO_2$ electrodes are higher than those of pure $PbO_2$ electrodes, which indicates that the porous structure can enlarge the active surface area. In addition, q* increases with the increase in manganese content in the electrodes. The total voltammetric charge values for $PbO_2$–$MnO_2$ (48.4%) electrodes are 2.5 times higher than that for the pure $PbO_2$ electrode (0.01123 C $cm^{-2}$).

**Table.** Influence of manganese content in $PbO_2$–$MnO_2$ electrodes on the electrochemical active surface area.

| Electrodes | $q^*_T$c(C $cm^{-2}$) |
|---|---|
| Pure $PbO_2$ electrodes | 0.01123 |
| $PbO_2$–$MnO_2$ (10.8%) electrodes | 0.01391 |
| $PbO_2$–$MnO_2$ (32.8%) electrodes | 0.01987 |
| $PbO_2$–$MnO_2$ (48.4%) electrodes | 0.02728 |

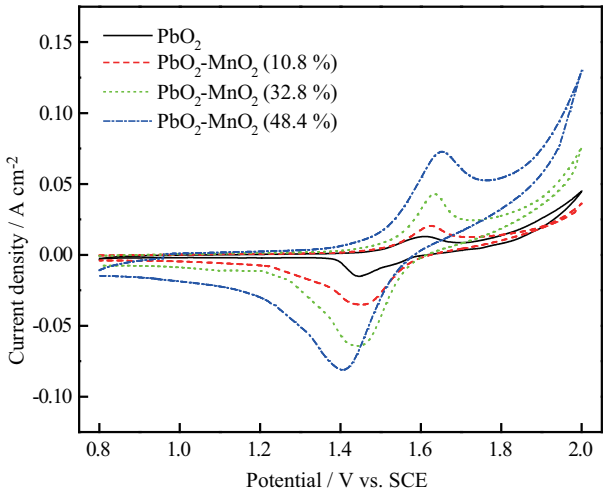


**Figure 5**. CV curves of pure $PbO_2$, $PbO_2$–$MnO_2$ (10.8%), $PbO_2$–$MnO_2$ (32.8%), and $PbO_2$–$MnO_2$ (48.4%) electrodes.

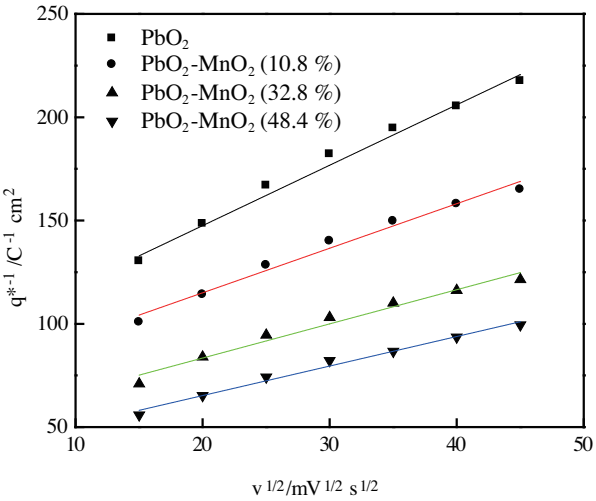


**Figure 6**. Relationship of $(q^*)^{-1}$ and $v^{1/2}$ for pure $PbO_2$, $PbO_2$–$MnO_2$ (10.8%), $PbO_2$–$MnO_2$ (32.8%), and $PbO_2$–$MnO_2$ (48.4%) electrodes.

The specific capacitances of pure $PbO_2$ and different $PbO_2$–$MnO_2$ electrodes were measured by galvanostatic charge–discharge test. Galvanostatic discharge curves of the above electrodes in 1 mol $L^{-1}$ $H_2SO_4$ solution at 0.5 A $g^{-1}$ are shown in Figure. 7a. All these electrodes show typical pseudocapacitive behavior with nonlinear discharge curves,[27] which is consistent with the cyclic voltammograms. The discharge process of $PbO_2$–$MnO_2$ electrodes can be divided into different stages. The first stage is a depression discharge curve and the slope decreases with the increase in manganese content in the electrodes. The fast drop can be ascribed to the ionic resistance of electrolyte and internal resistance of the electrodes.[28] The second stage is a discharge plateau. The plateau is prolonged with the increase in manganese content in the electrodes. The existence of plateaus shows the typical pseudocapacitive characteristics, which corresponds to the redox reaction process.[29] At the third stage, the discharge curves continue to decline.

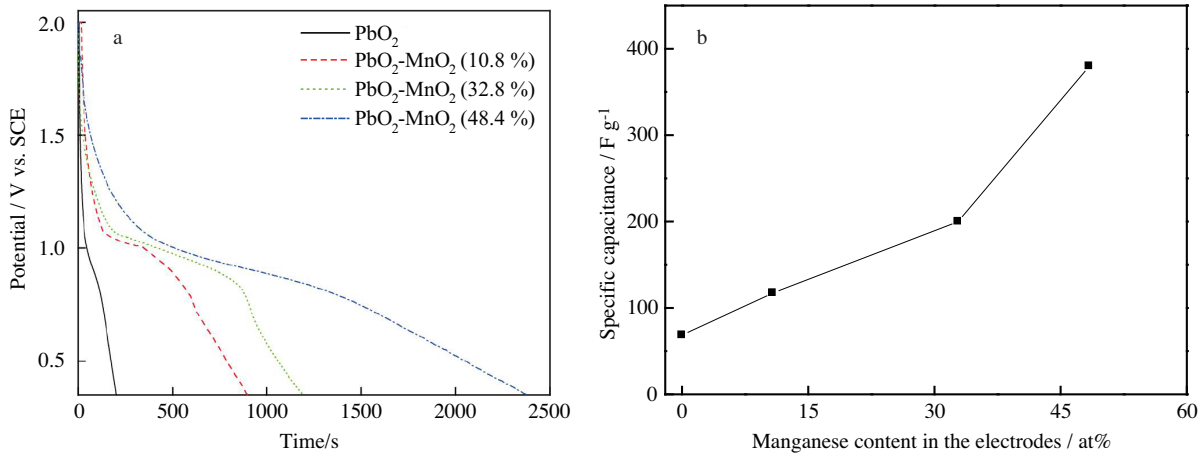


**Figure 7**. (a) The galvanostatic discharge curves of $PbO_2$, $PbO_2$–$MnO_2$ (10.8%), $PbO_2$–$MnO_2$ (32.8%), and $PbO_2$–$MnO_2$ (48.4%) electrodes at 0.5 A $g^{-1}$. (b) The influence of manganese content on the specific capacitance.

The specific capacitances of these electrodes can be obtained according to the following equation:

$$C = \frac{I \times \Delta t}{\Delta E \times m}, \tag{2}$$

where C is the specific capacitance (F $g^{-1}$), I is the discharge current (A), m is the electrode mass (g), $\Delta$E is the discharge potential window (V), and $\Delta$t is the discharge time (s). The obtained specific capacitance is shown in Figure 7b. Obviously, pure $PbO_2$ electrodes have lower specific capacitance values than $PbO_2$–$MnO_2$ electrodes, which is only 64.3 F $g^{-1}$. With the increase in manganese content, the specific capacitance of $PbO_2$–$MnO_2$ electrodes increases. The specific capacitance of $PbO_2$–$MnO_2$ (48.4%) electrodes could reach 374.5 F $g^{-1}$, which is also higher than that of $MnO_2$ prepared by electrodeposition methods (67 F $g^{-1}$).[30]

Figure 8a shows the galvanostatic discharge measurements of $PbO_2$–$MnO_2$ (48.4%) electrodes in 1 mol $L^{-1}$ $H_2SO_4$ solution with various current densities from 0.5 to 2.5 A $g^{-1}$. It can be observed that the discharge time of $PbO_2$–$MnO_2$ (48.4%) electrodes decreases gradually with the increase in discharge current densities, demonstrating the diffusion-controlled kinetics process for the electrode reactions on $PbO_2$–$MnO_2$ electrodes.[31] As shown in Figure 8b, when the discharge current density increased from 0.5 A $g^{-1}$ to 2.5 A $g^{-1}$, the specific capacitance of $PbO_2$–$MnO_2$ (48.4%) electrodes decreased from 374.5 F $g^{-1}$ to 84.8 F $g^{-1}$. The decrease in specific capacitance is mainly attributed to a limited accessible area for ion diffusion with the increase in current density.[32]

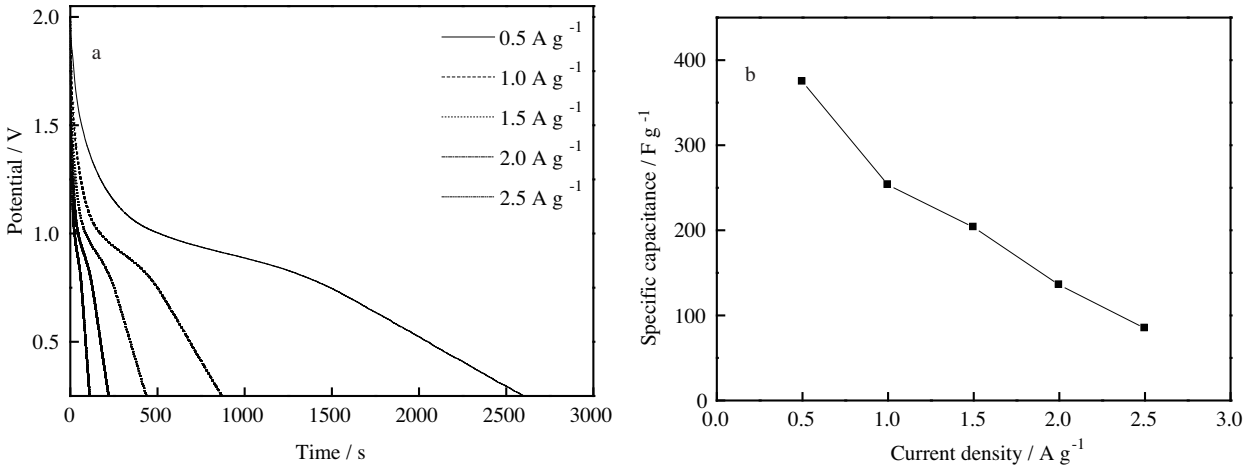


**Figure 8**. (a) Galvanostatic discharge curves of $PbO_2$–$MnO_2$ (48.4%) electrodes with different current densities; (b) Specific capacitances of $PbO_2$–$MnO_2$ (48.4%) electrodes at different current densities.

Figure 9 shows the electrochemical impedance spectroscopy (EIS) for the $PbO_2$–$MnO_2$ (48.4%) electrodes and pure $PbO_2$ electrodes, and the electrical equivalent circuit is also given in Figure 9 (inset). A straight line in the low frequency region and a semicircle part in the high frequency region were clearly observed. The equivalent circuit consists of bulk solution resistance $R_s$, charge transfer resistance $R_{ct}$, the Warburg resistance ($Z_w$) related to the diffusion of ions, and the constant phase element (CPE) to replace the double layer capacitance ($C_{dl}$).[33] The result shows that the charge transfer resistance ($R_{ct}$) of the $PbO_2$–$MnO_2$ (48.4%) electrodes (38.3 $\Omega$ $cm^{-2}$) is lower than that of the pure $PbO_2$ electrode (132.7 $\Omega$ $cm^{-2}$), indicating that the $PbO_2$–$MnO_2$ (48.4%) electrodes have much faster kinetics than the pure $PbO_2$ electrodes do, which benefits the supercapacitive performance of electrode materials.[34]

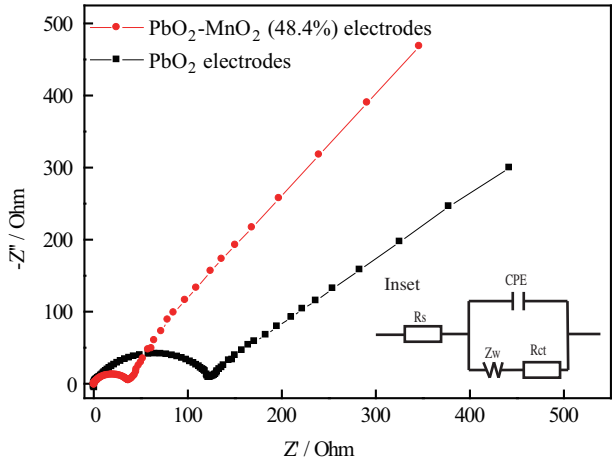


**Figure 9**. Nyquist plots of $PbO_2$–$MnO_2$ (48.4%) and $PbO_2$ electrodes in 1.0 mol $L^{-1}$ $H_2SO_4$ solution (the inset is the equivalent electric circuit for the EIS).

### 2.3. Discussion

The aforementioned results show that $PbO_2$–$MnO_2$ electrodes possess higher specific capacitance performance than pure $PbO_2$ electrodes do. It can be attributed to the following factors. First, the porous structure enlarges the electrochemical activity surface area and provides more active sites for the electrolyte ions in contact with the active material, such as lead dioxide and manganese dioxide, which is beneficial for utilizing the active materials.[24] Second, the high specific capacitance of $PbO_2$–$MnO_2$ electrodes can be ascribed to the synergetic effect between $PbO_2$ and $MnO_2$. $PbO_2$ can strengthen the conductivity of $MnO_2$ and $MnO_2$ can enhance the capacitance of $PbO_2$, which allows $MnO_2$ to store and release charge through the $PbO_2$.[12]

## 3. Experimental

$PbO_2$–$MnO_2$ electrodes were prepared by electrochemical codeposition methods in lead nitrate solution containing manganese nitrate. The electrolytic solution consisted of 0.2 mol $L^{-1}$ $Pb(NO_3)_2$, 0.01 mol $L^{-1}$ $HNO_3$, and different concentrations of $Mn(NO_3)_2$ (10, 30, and 50 mmol $L^{-1}$). The solution temperature was 30 °C and current density was 30 mA $cm^{-2}$. A Ti/$SnO_2$–$Sb_2O_3$ interlayer was prepared on a Ti sheet by thermal decomposition method.[35] A Ti/$SnO_2$–$Sb_2O_3$ interlayer of 1 $cm^2$ apparent surface area was used as the substrate for electrodeposition of $PbO_2$–$MnO_2$ electrodes. The Pb electrode was used as the cathode. The pure $PbO_2$ electrodes were also obtained under the same condition from an electrolyte without $Mn(NO_3)_2$.

A Supra 55VP FESEM was used to characterize the surface morphology of the $PbO_2$–$MnO_2$ electrodes. The structure of the $PbO_2$–$MnO_2$ electrodes was detected with a Bruker XRD. The grain sizes were calculated by Scherrer's formula. Apollo XV energy dispersive X-ray spectroscopy was employed to investigate the composition of the $PbO_2$–$MnO_2$ electrodes. XPS was conducted by a K-Alpha spectrometer (Thermo Fisher Inc.).

The supercapacitor was assembled with the $PbO_2$–$MnO_2$ electrode as positive electrode and the activated carbon electrode as negative electrode separated by a porous polymeric separator in 1 mol $L^{-1}$ $H_2SO_4$ solution. The mass of the $PbO_2$–$MnO_2$ electrode is 0.020 g. Cyclic voltammograms were measured by CHI 660D electrochemical workstation in 1 mol $L^{-1}$ $H_2SO_4$ solution. The working electrodes were $PbO_2$–$MnO_2$

electrodes (10 mm × 10 mm), while the counter and reference electrodes were activated carbon electrodes and saturated calomel electrodes, respectively. The GCD curves were investigated by CT3008 battery test system (China Neware Ltd); the positive electrode materials used $PbO_2$–$MnO_2$ electrodes and the negative electrode materials used activated carbon electrodes.

## 4. Conclusions

$PbO_2$–$MnO_2$ electrodes were prepared using electrochemical codeposition methods by the addition of manganese nitrate to lead nitrate solution. The manganese content in the $PbO_2$–$MnO_2$ electrodes increased with the increase in manganese ion concentration in the solution. $PbO_2$–$MnO_2$ electrodes exhibited a porous structure and the crystal size decreased with the increase in manganese content. The specific capacitance of $PbO_2$–$MnO_2$ (48.4%) electrodes can reach 374.5 F $g^{-1}$, which is far higher than that pure $PbO_2$ electrodes (64.3 F $g^{-1}$). The excellent specific capacitance can be ascribed to the porous structure and the synergy of lead dioxide and manganese dioxide.

## Acknowledgment

The project was supported by the National Natural Science Foundation of China (No. 21576065).

## References

1. Yan, J.; Qian, W.; Tong, W.; Fan, Z.; *Adv. Energy Mater.* **2014**, *4*, 157-164.
2. Wang, G.; Zhang, L.; Zhang, J. J. *Chem. Soc. Rev.* **2012**, *41*, 797-828.
3. Perret, P.; Khani, Z.; Brousse, T.; Bélanger, D.; Guay, D. *Electrochim. Acta* **2011**, *56*, 8122-8128.
4. Egan, D. R. P.; Low, C. T. J.; Walsh, F. C. *J. Power Sources* **2011**, *196*, 5725 -5730.
5. Sáez, V.; Marchante, E.; Díez, M. I.; Esclapez, M. D.; Bonete, P.; Lana-Villarreal, T.; García, J. G.; Mostany, J. *Mater Chem. Phys.* **2011**, *125*, 46-54.
6. Moncada, A.; Piazza, S.; Sunseri, C.; Inguanta, R. *J. Power Sources* **2015**, *215*, 181-188.
7. Yang, C. J.; Park, S. M. *Electrochim. Acta* **2013**, *108*, 86-94.
8. Velichenko, A. B.; Amadelli, R.; Gruzdeva, E. V.; Luk'Yanenko, T. V.; Danilov, F. I. *J. Power Sources* **2009**, *191*, 103-110.
9. Ghasemi, S.; Mousavi, M. F.; Karami, H.; Shamsipur, M.; Kazemi, S. H. *Electrochim. Acta* **2006**, *52*, 1596-1602.
10. Yu, N. F.; Gao, L. J. *Electrochem. Commun.* **2009**, *11*, 220-222.
11. Li, X. H.; Pletcher, D.; Walsh, F. C. *Chem. Soc. Rev.* **2011**, *40*, 3879-3894.
12. Dan, Y. Y.; Lin, H. B.; Liu, X. L.; Lu, H. Y.; Zhao, J. Z.; Shi, Z.; Guo, Y. P. *Electrochim. Acta* **2012**, *83*, 175-182.
13. Toupin, M.; Brousse, T., Bélanger, D. *Chem. Mater.* **2004**, *16*, 3184-3190.
14. Dalili, N.; Clark, M. P.; Davari, E.; Ivey, D. G. *J. Power Sources* **2016**, *328*, 318-328.
15. Cao, J. Y.; Li, X. H.; Wang, Y. M.; Walsh, F. C.; Ouyang, J. H.; Jia, D. C.; Zhou, Y. *J. Power Sources* **2015**, *293*, 657-674.
16. Yang, H. T.; Chen, B. M.; Liu, H. R.; Guo, Z. C.; Zhang, Y. C.; Li, X. L.; Xu, R. D. *Int. J. Hydrogen Energ.* **2014**, *39*, 3087-3099.
17. Rolison, D. R.; Long, J. W.; Lytle, J. C.; Fischer, A. E.; Rhodes, C. P.; Mcevoy, T. M.; Bourg, M. E.; Lubers, A. M. *Chem. Soc. Rev.* **2009**, *38*, 226-252.

18. Zhang, H. H.; Gu, J. N.; Tong, J.; Hu, Y. F.; Guan, B.; Hu, B.; Zhao, J.; Wang, C. Y. *Chem. Eng. J.* **2016**, *286*, 139-149.
19. Shmychkova, O.; Luk'Yanenko, T.; Amadelli, R.; Velichenko, A. *J. Electroanal. Chem.* **2014**, *717-718*, 196-201.
20. Guo, W. H.; Liu, T. J.; Jiang, P.; Zhang, Z. J. *J. Colloid Interface Sci.* **2015**, *437*, 304-310.
21. Yu, N. F.; Gao, L. J.; Zhao, S. H.; Wang, Z. D. *Electrochim. Acta* **2009**, *54*, 3835-3841.
22. Zhang, W. L.; Lin, H. B.; Kong, H. S.; Lu, H. Y.; Yang, Z.; Liu, T. T. *Electrochim. Acta* **2014**, *139*, 209-216.
23. Trasatti, S.; Petrii, O. A. *J. Electroanal. Chem.* **1992**, *327*, 353-376.
24. Montilla, F.; Morallón, E.; Battisti, A. D.; Vazquez, J. L. *J. Phys. Chem. B* **2004**, *108*, 5036-5043.
25. Ardizzone, S.; Fregonara, G.; Trasatti, S. *Electrochim. Acta* **1990**, *35*, 263-267.
26. Xu, L.; Li, M.; Xu, W. *Electrochim. Acta.* **2015**, *166*, 64-72.
27. Bai, Y.; Wang, R. R.; Lu, X. Y.; Sun, J.; Gao, L. *J. Colloid Interface Sci.* **2016**, *468*, 1-9.
28. Li, M.; Ma, K. Y.; Cheng, J. P.; Lv, D. H.; Zhang, X. B. *J. Power Sources* **2015**, *286*, 438-444.
29. Huang, K. J.; Zhang, J. Z.; Cai, J. L. *Electrochim. Acta* **2015**, *180*, 770-777.
30. Yang, J.; Lian, L. F.; Ruan, H. C.; Xie, F. Y.; Wei, M. D. *Electrochim. Acta* **2014**, *136*, 189-194.
31. Yang, X.; Qu, F. Y.; Niu, H.; Wang, Q.; Yan, J.; Fan, Z. J. *Electrochim Acta* **2015**, *180*, 287-294.
32. Guo, W. H.; Liu, T. J.; Jiang, P.; Zhang, Z. J. *J. Colloid Interface Sci.* **2015**, *437*, 304-310.
33. Li, H. L.; Jiang, L. X.; Cheng, Q. L.; He, Y.; Pavlinek, V.; Saha, P.; Li, C. Z. *Electrochim. Acta* **2015**, *164*, 252-259.
34. Li, Y. J.; Wang, G. L.; Ye, K.; Cheng, K.; Pan, Y.; Yan, P.; Yin, J. L.; Cao, D. X. *J. Power Sources* **2014**, *271*, 582-588.
35. Yao, Y. W.; Jiao, L. M.; Yu, N. C.; Guo, F.; Chen, X. *J. Solid State Electrochem.* **2016**, *20*, 353-359.